

Radio-frequency biasing of ion thruster grids

IEPC-2019-145

*Presented at the 36th International Electric Propulsion Conference
University of Vienna, Austria
September 15-20, 2019*

Trevor Lafleur*, Dmytro Rafalskyi† and Ane Aanesland‡
ThrustMe, Verrières-le-Buisson, Île-de-France, F-91370, France

Abstract: To ensure overall current balance, and ion beam space charge compensation, conventional gridded ion thrusters require an electron-emitting neutralizer. If instead a radio-frequency (RF) voltage is applied across the grids, and a capacitor is added to the external circuit, both electrons and ions can be extracted from the thruster and a neutralizer is no longer needed. In this paper, the fundamental operation of such a system is discussed, and the effect of the applied frequency is studied using analytical theory and particle-in-cell simulations. Initial charging of the capacitor leads to the formation of a DC self-bias voltage across the grids (in addition to the applied RF voltage) that allows continuous ion extraction and acceleration. By contrast, electrons only escape the thruster in bursts synchronized with the RF cycle when the applied voltage reaches a minimum. Both the self-bias voltage, and the plume plasma potential, self-consistently develop in such a way so as to ensure current conservation of the thruster. The applied frequency is a key system parameter, and if the RF period is less than approximately the ion transit time through the grids, good ion focusing can be obtained with no direct ion impingement of the accel grid. In addition, the resulting ion beam has a low divergence angle, and is sharply-peaked in velocity-space. For typical grid dimensions and ion beam current densities, the ion transit time restriction gives a lower frequency limit of about 10-15 MHz. As long as the applied frequency is above this limit, efficient ion acceleration can occur together with inherent thruster current balance, and ion beam space charge compensation.

*Research scientist, trevor.lafleur@thrustme.fr

†CTO, dmytro.rafalskyi@thrustme.fr

‡CEO, ane.aanesland@thrustme.fr

Nomenclature

A_{exit}, A_{walls}	= exit area, and area of the radial and back walls, of the upstream plasma source
A_d^a, A_h^a, A_u^a	= area of the downstream, hole, and upstream surfaces of the accel grid
A_d^s, A_h^s, A_u^s	= area of the downstream, hole, and upstream surfaces of the screen grid
C	= capacitance
e	= magnitude of the elementary charge
f	= applied RF frequency
$F(\varepsilon)$	= ion flux distribution function in energy units
I_0	= zeroth order modified Bessel function of the first kind
I_{beam}	= ion beam current
I_e, I_i	= electron and ion currents escaping the thruster
$I_{i,d}^a, I_{i,h}^a, I_{i,u}^a$	= ion current to the downstream, hole, and upstream surfaces of the accel grid
$I_{i,h}^s, I_{i,u}^s$	= ion current to the hole and upstream surfaces of the screen grid
J_e, J_i	= electron and ion current densities of the upstream bulk plasma
J_i^{CL}	= maximum ion current density from the Child-Langmuir law
L	= maximum axial length of the simulation domain
L_d, L_u	= accel grid-to-dielectric distance and upstream-to-screen grid distance
L_{eff}, L_g	= effective and physical intergrid separation distances
m, M	= electron and ion masses
n	= RF period index
n_g, n_u	= neutral gas density and upstream bulk plasma density
p_0	= neutral gas pressure
Q_e, Q_i	= total electron and ion charge collected on the accel grid over an RF period
r, R	= radial coordinate and maximum radial length of the simulation domain
r_a, r_s	= radius of the accel and screen grid apertures
t	= time variable
t_a, t_{die}, t_s	= thickness of the accel grid, downstream dielectric, and screen grid
T	= RF period
T_e, T_g, T_i	= electron temperature, neutral gas temperature, and ion temperature
\bar{v}_e	= electron thermal speed
V_{pa}	= potential between the plume and accel grid
V_{rf}	= applied RF voltage amplitude
V_{sa}	= potential between the screen and accel grids
V_{sb}	= self-bias voltage
V_{sheath}	= Sheath potential between the upstream bulk plasma and the screen grid
z	= axial coordinate of the simulation domain
α	= ion accel grid-to-beam current ratio
ΔI_{die}	= net current to the downstream dielectric boundary
ΔV_{plume}	= maximum change in plume potential over an RF period
$\varepsilon_0, \varepsilon_r$	= permittivity of free space and relative dielectric permittivity
ε_{ave}	= average ion beam energy
ζ	= generic function argument
η_i	= ion-grid transparency
θ_{ave}	= average ion beam divergence angle
σ_{cex}	= ion-neutral charge-exchange cross-section
σ_ε	= standard deviation of the ion beam flux-distribution function
τ	= ion transit time through the grids
ω	= applied RF angular frequency

I. Introduction

Gridded ion thrusters (GITs) are some of the most mature electric propulsion systems and have successfully been used in space for more than 50 years.¹ While many different GIT designs are in operation, the basic configuration consists of a discharge chamber and a set of DC biased grids. Neutral propellant gas (usually xenon) is injected into the discharge chamber, and a plasma is created using either a DC hollow cathode (which supplies high-energy electrons), inductive fields from a radio-frequency (RF) antenna (wrapped around the outside of a dielectric discharge chamber), or microwaves (which heat electrons through electron cyclotron resonance in the presence of a strong DC magnetic field). By applying a voltage across the grids (which contain many hundreds or thousands of small apertures), ions are extracted and accelerated to generate thrust. Since plasma generation is largely de-coupled from the ion acceleration stage, gridded ion thrusters can achieve very high specific impulses and thruster efficiencies because of the large voltage that can be applied across the grids.

As the polarity of the accelerating voltage is chosen to extract positive ions, plasma electrons in the discharge chamber are blocked and cannot escape. However, continual positive ion loss would lead to rapid charging of the thruster/satellite, as well as uncompensated ion space charge in the thruster plume. This uncompensated space charge builds up and increases the plume potential until eventually the ion beam stalls, and ions are reflected back towards the grids.² In order to prevent this, conventional GITs make use of an electron-emitting thermionic or hollow cathode (known as a neutralizer), placed externally to the thruster, and in close proximity to the last grid.¹ Electron emission from this neutralizer serves both to ensure overall current balance of the thruster/satellite, and to produce a quasi-neutral plume by compensating the positive ion beam space charge.

While neutralizers are a very well-understood and established technology, they nonetheless represent an additional component that is required in GITs, and if the neutralizer fails, the thruster may no longer be able to operate correctly.³ Neutralizers also require additional power supplies, and for hollow cathode systems (which represent the current state-of-the-art¹), additional propellant gas feed and control systems. This extra hardware increases the complexity of the thruster, as well as the mass and volume of the overall propulsion system; factors that can limit miniaturisation of such thrusters for small satellite applications.

The need for a separate neutralizer can be eliminated if electrons from the plasma in the discharge chamber itself could be extracted together with the ions. One method for achieving this (first proposed in Refs.⁴⁻⁶ and subsequently improved on in Refs.^{7,8}) is to replace the DC accelerating voltage with an RF voltage, and connecting a special capacitor to the grids. Charging of this capacitor leads to the formation of a DC self-bias voltage (in addition to the applied RF voltage), allowing ions to be continually extracted and accelerated as in conventional GITs, while electrons escape in pulses when the RF voltage reaches a minimum. This concept has been demonstrated experimentally,⁷ and the basic hypothesised operating principles confirmed theoretically and numerically.⁹ In this paper, we review the fundamental operation of such a thruster, and numerically investigate the effect of the applied frequency, which represents a critical parameter for ensuring good ion extraction and plume neutralization.

II. Fundamental physics of RF biased grids

The inspiration for RF biasing of ion thruster grids comes from the semiconductor industry. Here, RF biased parallel plate electrodes are widely used to generate uniform plasmas over large area for deposition and etching processes. Neutral gas is injected between the electrodes, and breakdown occurs when a large enough RF voltage is applied. As power is coupled to the discharge capacitively, these sources are known as capacitively coupled plasma (CCP) reactors.¹⁰ In contrast to the usual floating DC sheath that forms at the interface between a plasma and a bounding surface, the RF sheath near each electrode in a CCP is more complex, with both the sheath width, and the amplitude of the potential drop, varying throughout the RF cycle.¹⁰⁻¹³

Because plasma sheaths can carry a net charge, they can be modelled as a capacitor. Since capacitance is directly proportional to the area of a capacitor, RF electrodes in CCPs with different areas (i.e. asymmetric CCPs) will have different capacitances, and consequently different RF impedances. This difference in impedance produces a voltage divider effect, and the amplitude of the voltage drop of the sheath at the smaller electrode will be larger. Because of this, the time-averaged voltage between the bulk plasma and the sheath at the smaller area electrode will be larger than the time-averaged voltage between the plasma

and the larger area electrode.^{10–12} If a capacitor is connected in series to one of the electrodes and the RF power generator in the external circuit, this voltage difference sets up a self-bias voltage at the smaller area electrode with respect to the larger area electrode. Physically, this self-bias forms due to charging by electrons and ions which strike the electrode, and equilibrium is reached once the electron and ion currents are equal (no conduction current can flow through a capacitor). A schematic of an asymmetric CCP reactor is shown in Fig. 1 (a).

A self-bias is also generated when an RF voltage is applied across the grids of an ion thruster and a capacitor added to the external circuit.^{7–9} A schematic of such an RF biased thruster is shown in Fig. 1 (b). Initially at startup the self-bias is zero, and during one half of the RF cycle a large electron current escapes. Some of these electrons strike the accel grid, and charging of the bias capacitor occurs. This forms a DC self-bias voltage that shifts the applied RF voltage, and during the next RF cycle, the electron current that escapes is reduced. Charging of the bias capacitor continues in this way until the electron and ion currents to the accel grid are equal. If the grid dimensions and the applied frequency are correctly chosen, then ions are well focused through the grids and the only ion current to the accel grid comes from low-energy ions produced predominantly in the near-plume region by either charge-exchange collisions, or ionization caused by the escaping electrons.⁹

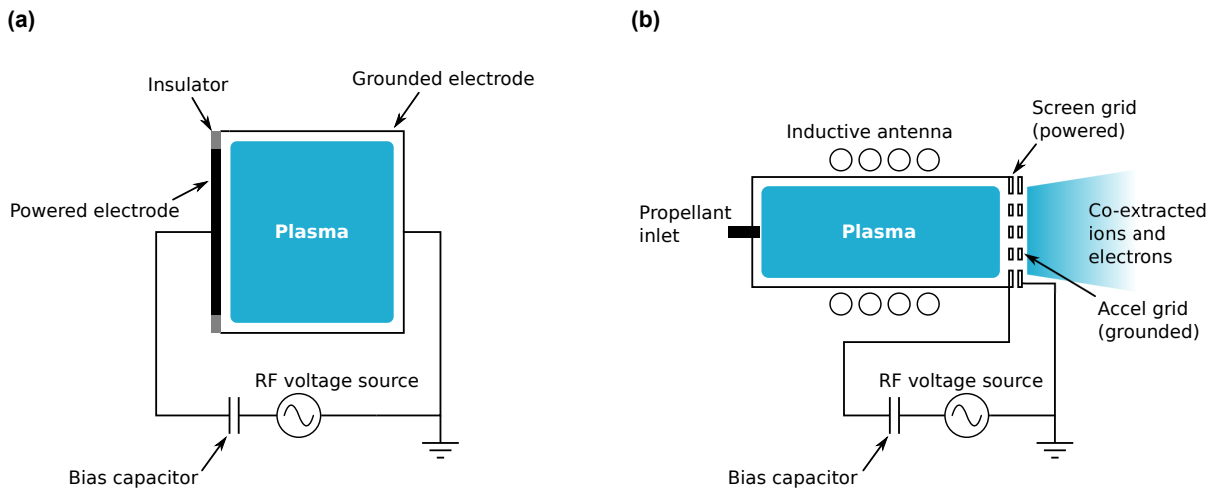


Figure 1. Schematic showing (a) an asymmetric CCP plasma reactor, and (b) an ion thruster with RF biased acceleration grids.

Although the electron and ion currents to the accel grid determine the self-bias voltage, this alone does not guarantee that the electron and ion currents *escaping* the thruster are equal, nor that the ion beam space charge is compensated. Particle-in-cell (PIC) simulations⁹ however, show that a potential well forms downstream of the accel grid; effectively trapping low-energy electrons and producing a quasi-neutral plume. The potential drop between the near-plume region and the far-field self-consistently adjusts so that the current of escaping high-energy electrons is equal to the ion beam current. Similarly, the potential drop between the near-plume region and the accel grid self-consistently adjusts until the electron current escaping the thruster is equal to the ion beam current and any backstreaming electron current. Experimental measurements have shown that the plume can indeed be well neutralized in RF biased ion thrusters.^{7, 8, 14}

With the basic operation of RF biased thrusters discussed above, we consider now some important theoretical relations. By requiring the net electron and ion currents to the screen grid to be equal, an expression for the sheath potential between the upstream plasma source and the screen grid, V_{sheath} , can be derived⁹

$$V_{sheath} = T_e \left\{ \frac{1}{2} \ln \left(\frac{M}{2\pi m} \right) - \ln \left[\frac{(1 - \eta_i) A_{exit} + A_{walls}}{A_u^s + A_h^s + A_{walls}} \right] \right\} \quad (1)$$

where T_e is the electron temperature, m and M are the electron and ion masses respectively, A_{exit} is the exit area of the upstream plasma source, A_{walls} is the area of the radial and back walls of the upstream plasma source, η_i is the effective screen grid transparency to ions, and A_h^s and A_u^s are the hole and upstream

surface areas of the screen grid. Similarly, by requiring the net electron and ion currents to the accel grid to be equal over an RF period at equilibrium, an expression for the self-bias voltage, V_{sb} , is obtained⁹

$$V_{sb} = T_e \left\{ \ln \left[I_0 \left(\frac{V_{rf}}{T_e} \right) \right] - \ln \left[\frac{\alpha \eta_i (A_u^s + A_h^s)}{(1 - \eta_i) (A_u^a + A_h^a)} \right] \right\} \quad (2)$$

Here V_{rf} is the applied voltage amplitude, I_0 is the zeroth order modified Bessel function of the first kind, $\alpha \approx n_g \sigma_{ceex} L_d$ is the ratio of the ion current to the accel grid to the ion beam current with n_g the neutral gas density, σ_{ceex} the ion-neutral charge-exchange cross-section, L_d a characteristic length of the order of the downstream distance within which ion beams from adjacent apertures merge, and A_h^a and A_u^a are the hole and upstream surface areas of the accel grid. For approximate estimates of the self-bias, we note that under typical operating conditions of interest (such as $V_{rf} \sim 1000$ V and $T_e \sim 5$ eV), $V_{rf} \gg T_e$. Performing a large argument expansion of the modified Bessel function in Eq. 2 we obtain

$$I_0(\zeta) \approx \frac{e^\zeta}{\sqrt{2\pi\zeta}} \quad (3)$$

Thus Eq. 2 becomes

$$V_{sb} \approx T_e \left\{ \frac{V_{rf}}{T_e} - \frac{1}{2} \ln \left(\frac{2\pi V_{rf}}{T_e} \right) - \ln \left[\frac{\alpha \eta_i (A_u^s + A_h^s)}{(1 - \eta_i) (A_u^a + A_h^a)} \right] \right\} \approx T_e \left\{ \frac{V_{rf}}{T_e} \right\} = V_{rf} \quad (4)$$

Here we have neglected the logarithmic terms in the last two steps, which are much smaller than the first term. Therefore, the self-bias voltage is approximately equal to the applied RF voltage amplitude. An important observation of Eq. 2 (and Eq. 4) is that the self-bias is independent of the applied RF frequency for a sinusoidal waveform.

Although the self-bias is independent of the applied frequency, the frequency is still expected to be important for both ion focusing, and plume neutralization. This can be seen as follows. Consider the DC Child-Langmuir law given by

$$J_i^{CL} = \frac{4\epsilon_0}{9} \sqrt{\frac{2e}{M}} \frac{V_{sa}^{3/2}}{L_{eff}^2} \quad (5)$$

where J_i^{CL} is the maximum ion current density that can be extracted between the grids, ϵ_0 is the permittivity of free space, e is the elementary charge (we assume singly-charged ions), V_{sa} is the voltage across the screen and accel grids, and $L_{eff} = \sqrt{(L_g + t_s)^2 + r_s^2}$ with L_g the physical intergrid separation distance, t_s the screen grid thickness, and r_s the radius of the apertures in the screen grid. Although Eq. 5 does not directly apply to RF biasing, we can nonetheless make the following observation: if the applied frequency is very low, then during those moments of the RF period when the voltage is low, the Child-Langmuir current density is lower than at those moments when the voltage is high. Thus, ions may not be well focused through the grids for low frequencies. We can estimate the lower frequency limit by calculating the ion transit time through the grids. Considering ions starting from rest, and using the approximation in Eq. 4, the transit time, τ , is

$$\tau \approx \sqrt{\frac{2L_{eff}^2 M}{eV_{rf}}} \quad (6)$$

If the RF period is larger than this transit time, then ions will more easily be able to respond to variations in the voltage, whereas if the RF period is much smaller than the transit time, temporal variations will be too quick for the ions to respond to and they will see only a time-averaged field. Equating the ion transit time to the maximum acceptable RF period, T , we can establish the following frequency criterion

$$f > \sqrt{\frac{eV_{rf}}{2L_{eff}^2 M}} \quad (7)$$

For xenon ions, an applied voltage of the order of 1000 V, and an effective grid spacing between about 1.25 - 2 mm, Eq. 7 gives a lower frequency limit of between 10 - 15 MHz.

A second frequency constraint is imposed by the level of downstream neutralization of the plume. Considering the thruster/satellite to have a capacitance relative to space or the surroundings of C , then the change in plume potential over an RF period, ΔV_{plume} , is given by

$$\Delta V_{plume} = \frac{1}{C} \int_0^t dt (I_i + I_e) \quad (8)$$

Here t is time, and I_i and I_e are the net ion and electron currents escaping the thruster. Since electrons are only lost during a narrow portion of the RF cycle, the total change in potential from ion loss between these pulses can be estimated as

$$\Delta V_{plume} \approx \frac{TI_i}{C} = \frac{I_i}{fC} \quad (9)$$

Thus, the lower the applied frequency, the higher the change in plume potential. For a maximum change of potential of 100 V, an ion beam current of 100 mA, and a capacitance of the order of 100 pF, the minimum required frequency is about 10 MHz. For the conditions chosen here, this is similar to the frequency limit for the ion transit time restriction, and again highlights the importance of the applied frequency. In Section IV, we use PIC simulations to study the effect of the applied frequency on ion focusing and plume neutralization in more detail.

III. Description of simulations

The PIC simulations used here are based on the model previously described⁹ which uses the XOOPIC code.¹⁵ The simulation domain, which models a single set of screen and accel grid holes in cylindrical coordinates, is shown in Fig. 2, together with the relevant boundary conditions. The accel grid and the downstream right-hand side (RHS) boundary are both grounded, the potential on the screen grid is, $V_{sb} + V_{rf} \sin \omega t$, and the potential on the upstream left-hand side (LHS) boundary is, $V_{sheath} + V_{sb} + V_{rf} \sin \omega t$. Here V_{sheath} is the potential drop between the upstream LHS boundary and the screen grid. Because of the bias capacitor connected to the grids (see Fig. 1 (b)), no net conduction current can flow to the screen or accel grids over an RF period once equilibrium has been reached. To satisfy these constraints, both the sheath potential drop, V_{sheath} , and the self-bias voltage, V_{sb} , are self-consistently adjusted in the simulation until the total electron and ion current to the screen grid, and separately also the accel grid, are equal over an RF period. This is achieved by recording the total charge collected by each of the grids over an RF period, and then adjusting the electrode potential. For example, the self-bias voltage is updated according to

$$V_{sb}^{n+1} = V_{sb}^n + \frac{1}{C} (Q_i^n - Q_e^n) \quad (10)$$

where V_{sb}^{n+1} is the new self-bias, V_{sb}^n is the old self-bias, C is a parameter (which plays the role of the capacitance of the bias capacitor), and Q_i^n and Q_e^n are the total ion and electron charges collected by the accel grid over the n -th RF period. In contrast to the simulations performed previously,⁹ a thin dielectric layer has been placed in front of the RHS boundary in the present work. This introduces a small capacitance between the thruster and any surrounding vacuum chamber (or space), and allows the thruster to float relative to the surroundings. It is also important for modelling the plume temporal variation for frequencies below about 10 MHz.

Both electrons and ions are treated as discrete particles, while collisions with neutral xenon gas are included using a standard Monte Carlo collision algorithm. Collision processes include ionization, excitation, and elastic scattering for electrons (with cross-sections taken from Ref.¹⁶), and charge-exchange and elastic scattering for ions (with cross-sections taken from Ref.¹⁷). The neutral gas is assumed to be uniform throughout the simulation domain with a pressure of 0.15 mTorr, and a temperature of 300 K. Ions and electrons are injected at the upstream LHS boundary, while all particles are specularly reflected from the cylindrical axis (which forms the lower simulation boundary), as well as the upper boundaries between the grids. Particles that strike the screen and accel grids, the upstream LHS boundary, and the downstream dielectric, are absorbed and removed. The initial injected ion velocity is equal to the Bohm velocity, while the initial ion temperature is 0.025 eV, and the injected current density is 35 Am⁻². The upstream plasma source (which is not modelled) is assumed to be quasi-neutral, and thus the injected electron current is

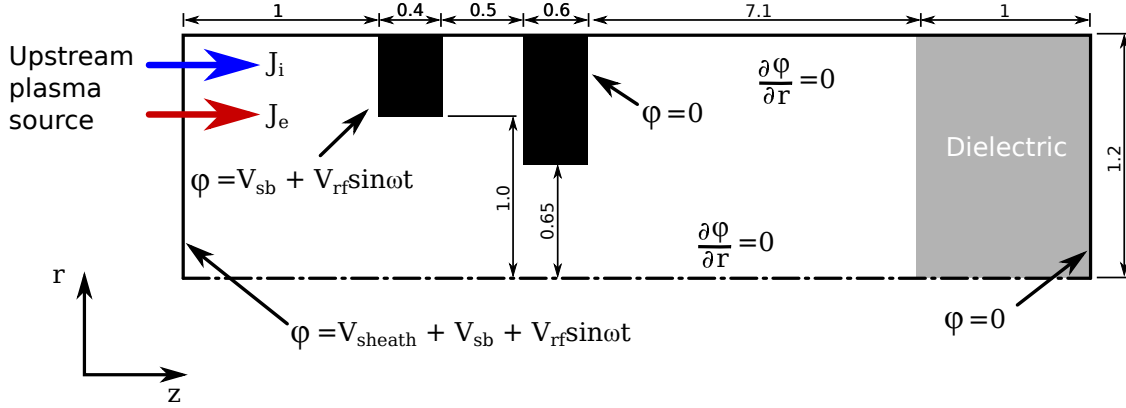


Figure 2. Schematic showing the PIC simulation domain and relevant dimensions. Drawing not to scale. All dimensions in mm.

approximated as, $J_e = \frac{1}{4}en_u\bar{v}_e$, which is a factor, $\sqrt{\frac{M}{2\pi m}}$, higher than the ion current, and where n_u is the upstream plasma density, and \bar{v}_e is the electron thermal speed. The initial injected electron temperature is 5 eV. Table 1 lists all of the relevant operating conditions and dimensions used in the simulations.

Table 1. Simulation operating conditions and dimensions.

Parameter	Value
RF frequency, f [MHz]	5 - 40
Injected ion current density, J_i [Am^{-2}]	35
Injected electron current density, J_e [Am^{-2}]	6830
Initial electron temperature, T_e [eV]	5
Initial ion temperature, T_i [eV]	0.025
RF voltage amplitude, V_{rf} [V]	500 - 2500
Xenon gas pressure, p_0 [mTorr]	0.15
Xenon gas temperature, T_g [K]	300
Relative dielectric permittivity, ϵ_r	10
Screen grid hole radius, r_s [mm]	1.0
Accel grid hole radius, r_a [mm]	0.65
Screen grid thickness, t_s [mm]	0.4
Accel grid thickness, t_a [mm]	0.6
Dielectric thickness, t_{die} [mm]	1.0
Intergrid separation, L_g [mm]	0.5
Upstream-to-screen grid distance, L_u [mm]	1.0
Accel grid-to-downstream distance, L_d [mm]	7.1
Total radial simulation length, R [mm]	1.2
Total axial simulation length, L [mm]	10.6

The simulations use a time step of 5×10^{-12} s, and a mesh size of 32×64 points (with a linearly increasing grid spacing in the axial direction). Between about 200 000 - 350 000 macroparticles per species are used, which gives an average of about 100 - 150 particles per cell per species.

IV. Influence of applied frequency

A. Upstream sheath potential and self-bias

Simulation equilibrium is typically reached after about 2 - 3 μs (which corresponds to of the order of 10 RF periods), but to ensure good convergence, simulations are run for a total of about 40 μs (of the order of 200 RF periods). Figure 3 shows an example of simulation convergence for a frequency of 20 MHz and an RF voltage amplitude of 1000 V. All other parameters are listed in Table 1. Figure 3 (a) and (b) shows the evolution of the upstream sheath potential and the self-bias voltage across the grids, while Fig. 3 (c) shows the total current to the downstream dielectric boundary. Once equilibrium is reached, the sheath potential and self-bias show good convergence, and the time-averaged electron and ion current to the dielectric is zero, as expected (i.e. no further charging occurs). The equilibrium values of the sheath potential and the self-bias voltage are in excellent agreement with the theoretical predictions from Eqs. 1 and 2 (red dashed lines in Figs. 3 (a) and (b)).

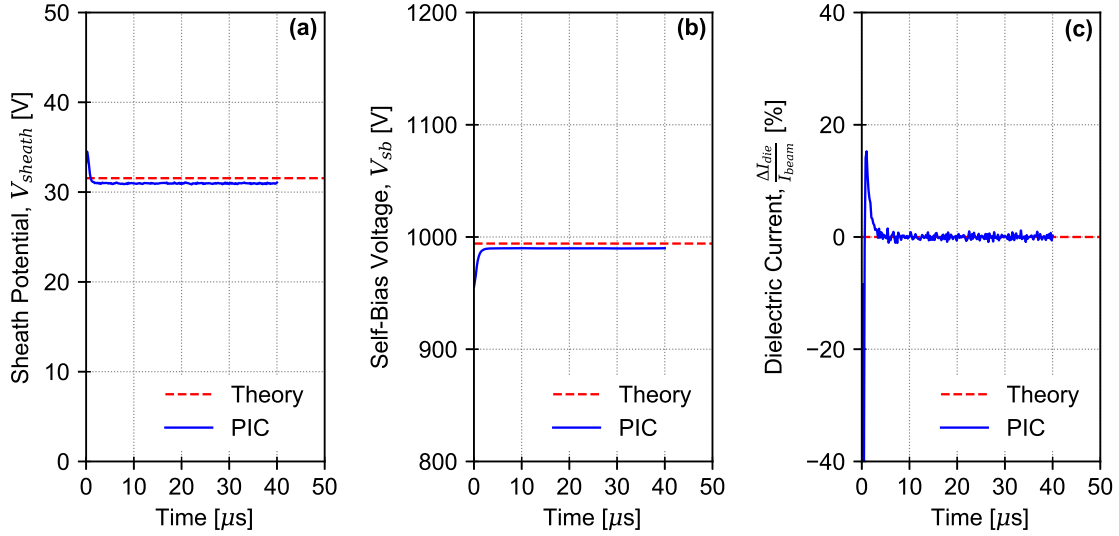


Figure 3. (a) Upstream sheath potential, (b) self-bias voltage, and (c) normalized electron and ion current to the downstream dielectric, as a function of time for an applied frequency of 20 MHz and an RF voltage amplitude of 1000 V. The horizontal red dashed lines in (a)-(c) show the expected theoretical values at equilibrium.

Based on the theoretical relations presented in Section II, both the upstream sheath potential, and the self-bias voltage, are expected to be independent of the applied RF frequency. Figure 4 shows the sheath potential and self-bias obtained from the simulations once equilibrium has been reached for a range of frequencies between 5 - 40 MHz (and an RF voltage amplitude of 1000 V). The theoretically expected values have been determined from Eqs. 1 and 2 (for accuracy, the value of α in Eq. 2 has been taken from the simulations themselves). The theory is found to be in excellent agreement with the simulation results. Over the frequency range tested, the simulations agree with the theory for the sheath voltage to within about 3 %, and around 0.5 % for the self-bias voltage, Furthermore, the simulations confirm that the sheath and self-bias voltages are largely independent of the applied frequency. The sheath voltage shows a slight decrease with decreasing frequency, which can be attributed to reduced ion focusing and increased ion current to the screen grid (see Section IV B). Similarly, there is a slight variation of the self-bias with frequency caused by the change in ion current to the accel grid with applied frequency.

B. Ion focusing

An important consideration in GIT design is the correct focusing of the ion beam through the grids.^{1,2} In particular, grid dimensions and applied voltages must be chosen so that direct ion impingement of the accel grid is avoided, as this would lead to rapid sputter erosion.¹⁸⁻²⁰ For RF biased grids, the applied frequency is an additional parameter that must now also be considered. The effect of the applied frequency on ion

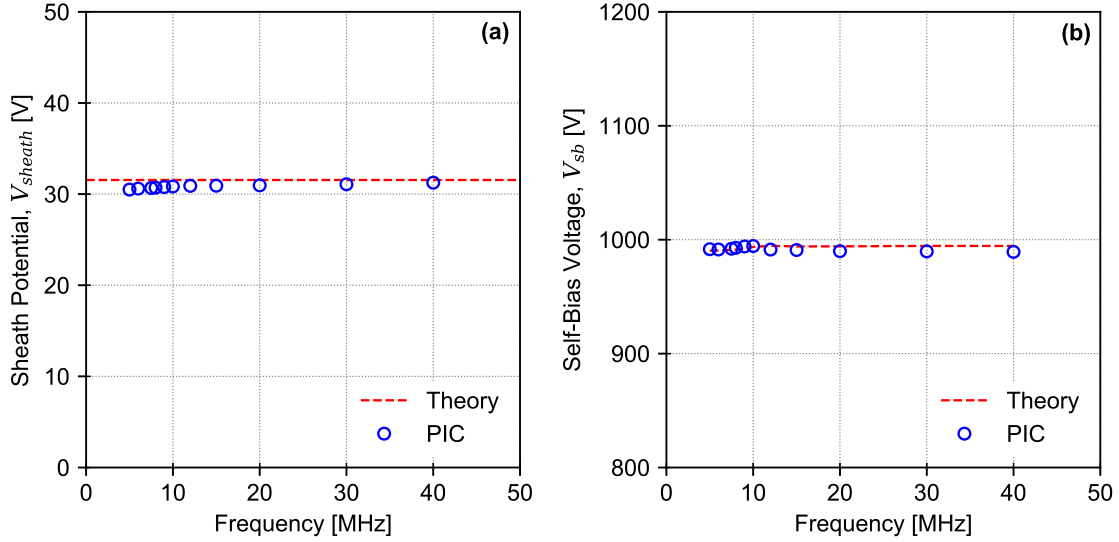


Figure 4. (a) Upstream sheath potential, and (b) self-bias voltage, as a function of the applied RF frequency. The red dashed curves in (a)-(b) show the expected theoretical values at equilibrium. The RF voltage amplitude is 1000 V.

focusing can be quantified by recording the time-averaged ion current to the screen and accel grids. For the screen grid, ions are only lost on the upstream and hole surfaces; no ions are lost on the downstream grid surface at any frequency. Figure 5 shows the ion current to the upstream and hole surfaces of the screen grid as a function of the applied frequency.

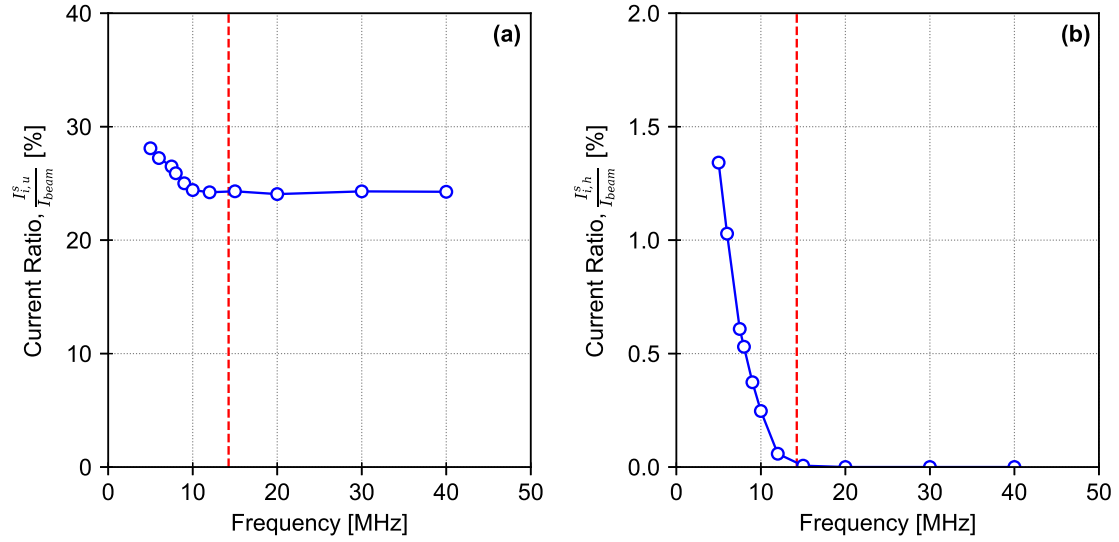


Figure 5. Ion current (normalized by the total beam current) to the (a) upstream and (b) hole surfaces of the screen grid as a function of the applied RF frequency. The vertical red dashed lines in (a)-(b) show the frequency (from Eq. 7) at which the ion transit time through the grids is equal to the RF period. The RF voltage amplitude is 1000 V.

In Fig. 5 (a) and (b), it is seen that as the applied frequency is increased, the ion current to both the upstream, and hole, surfaces of the screen grid decrease until saturating for frequencies above about 15 MHz. This demonstrates that ion focusing in RF biased gridded thrusters improves as the frequency is increased. It is also observed that saturation of the ion currents occurs close to the frequency predicted by Eq. 7. Thus, the physical interpretation of the results is clear: at low frequencies, ions can more easily respond to

the time-varying accelerating voltage, and in particular, when the voltage is low during one half of the RF cycle, new ions entering the sheath in front of the screen grid are no longer as strongly focused as those ions entering when the voltage is high. This reduced focusing causes more ions to strike the upstream screen grid surface, as well as the hole surface. As the applied frequency increases, the ion inertia increasingly prevents them from responding to the time-varying voltage, and so they begin to see just a time-average, similar to that which would occur in conventional DC biased GITs.

While reduced focusing increases the ion current to the screen grid, the ions which strike this grid still have a low energy. By contrast, ions which strike the accel grid will on average have a much higher energy, and thus ion impingement of the accel grid is arguably more important. Figure 6 shows the ion current to the upstream, hole, and downstream surfaces of the accel grid as a function of the applied frequency.

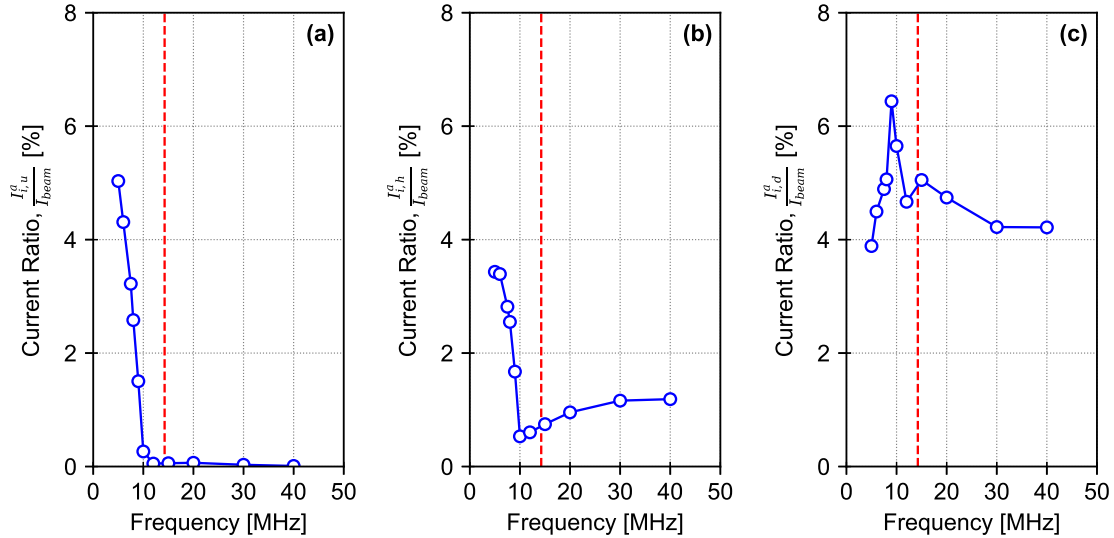


Figure 6. Ion current (normalized by the total beam current) to the (a) upstream and (b) hole, and (c) downstream surfaces of the accel grid as a function of the applied RF frequency. The vertical red dashed lines in (a)-(c) show the frequency (from Eq. 7) at which the ion transit time through the grids is equal to the RF period. The RF voltage amplitude is 1000 V.

Direct ion impingement of the upstream grid surface is observed for frequencies below about 12 MHz in Fig. 6 (a) and (b). At the lowest frequency of 5 MHz, the impingement current on the upstream grid surface is about 5%, and the ion bombarding energy (not shown) is many hundreds of eV. For frequencies above 12 MHz (which is close to that predicted by the ion transit time criterion in Eq. 7), impingement of the upstream accel grid surface is completely eliminated, and the remaining ion current comes from downstream ions that backstream into the thruster (mainly charge-exchange ions or any ions produced by downstream ionization). Similarly, for frequencies above about 12 MHz, direct impingement of the hole accel grid surface stops. Interestingly though, increasing the frequency above 12 MHz leads to an increase of the hole current. This current however comes from downstream ions, and occurs because of a complex interplay between a number of factors. For example, as the frequency increases, ion focusing improves and this both increases the ion beam current that is extracted through the grids (and thus a higher number of charge-exchange ions can now be produced), and also reduces the effective divergence of the ion beam. At low frequencies, the ion space charge causes significant expansion of the ion beam. This results in increased divergence, and consequently more of the charge-exchange ions that are produced tend to be lost on the downstream accel grid surface. As the frequency increases, the space charge effects are reduced, and the beam becomes more collimated with a lower divergence. Thus, fewer of the charge-exchange ions produced are lost at the downstream accel grid surface, while more are lost to the hole surface. This explains why the ion current to the hole surface increases with higher frequencies, but the ion current to the downstream surface decreases. In addition, the different plume potentials (see Section IV D) lead to different electron energy distribution functions which change the level of downstream ionization.⁹

The effect of the applied frequency on ion focusing can be most clearly seen by observing ion phase space plots at different moments during the RF cycle. Figure 7 shows such plots at the RF phases indicated in

the small inset figures for a low frequency of 5 MHz, and a high frequency of 40 MHz. At 5 MHz, the plume shows only a single dominant density perturbation or "beam front" (Fig. 7 (a)), and as the RF cycle progresses (Figs. 7 (c) and (e)), this front continues to move downstream, spreading and diffusing in the process. When the applied RF voltage is low (Fig. 7 (e)), the ion space charge in the grids counteracts the now reduced accelerating electric field, and ion focusing is lost. This can clearly be seen by the large group of ions that span almost the entire thickness of the screen grid. When the applied RF voltage once again increases (Fig. 7 (g)), this previous reduction in focusing then causes a significant fraction of ions to be directly accelerated into the upstream and hole surfaces of the accel grid. These ions have an energy of many hundreds of eV, and would lead to rapid erosion of the accel grid.

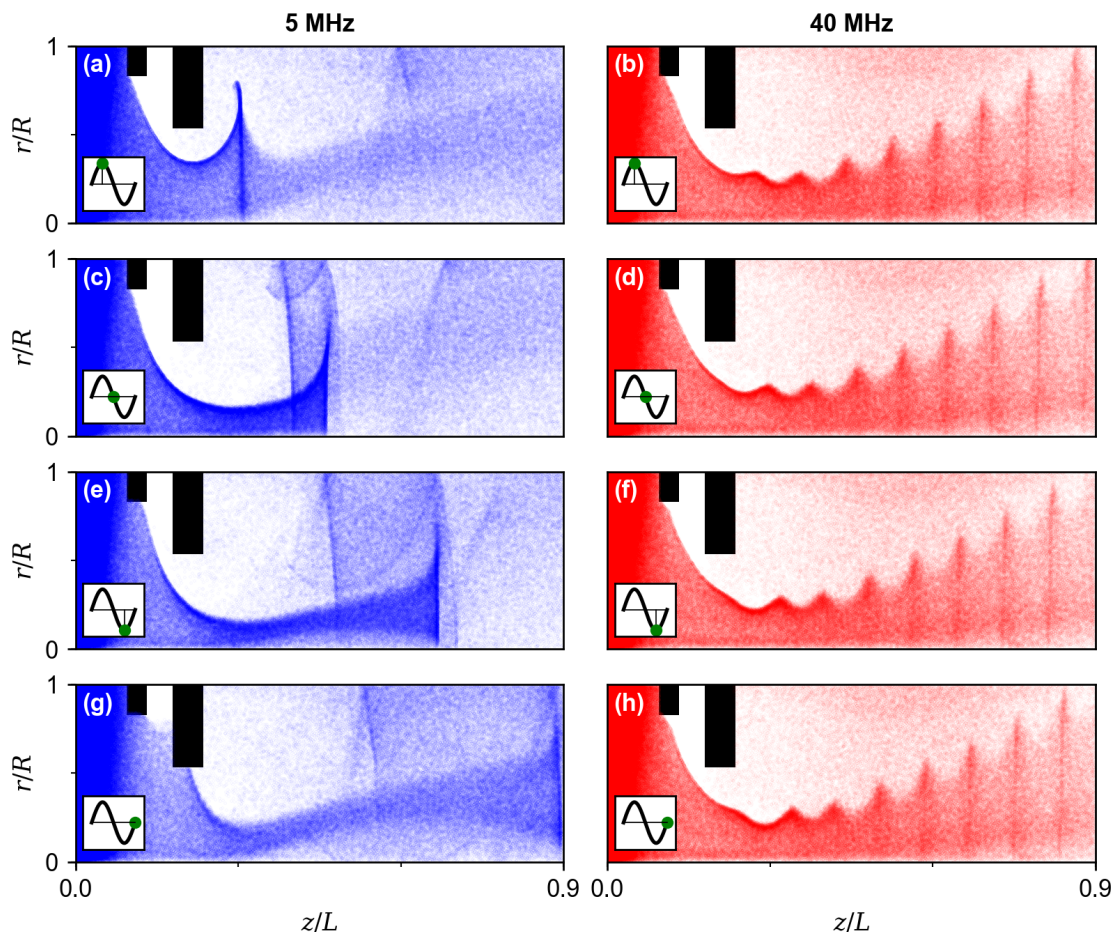


Figure 7. Spatial distribution of ions within the simulation domain at the RF phases indicated by the small inset figures. The left column shows results at an applied frequency of 5 MHz, while the right column shows results for 40 MHz. The black rectangles denote the location of the grids. The RF voltage amplitude is 1000 V.

At 40 MHz, the ion transit time is much longer than the RF period, and as many as eight distinct density perturbations or "peaks" can now be seen in the downstream plume (Fig. 7 (b)). These peaks propagate downstream as the RF phase proceeds (Figs. 7 (d), (f), and (h)), although little difference in the ion trajectories between the grids and in the plume region are observed. When the RF voltage collapses (Fig. 7 (f)), a very slight perturbation to the ion trajectories is seen, but as the frequency is much higher now, these ions are not able to travel very far before the RF voltage once again increases (Fig. 7 (h)). Thus, any perturbations are essentially smoothed out, and ion focusing averaged over the RF period is well maintained.

C. Ion beam velocity distribution function

In addition to affecting ion focusing through the grids, the applied frequency has a significant effect on the velocity distribution of the ion beam. Figure 8 shows the ion flux distribution function (displayed in terms of energy units) on the downstream dielectric boundary at each of the applied frequencies indicated. At low frequencies, the distributions are very broad in energy and have a complicated shape with many distinct peaks. As the ion transit time through the grids at these low frequencies is less than the RF period, the ions can follow any temporal variations in the applied RF voltage, and thus, depending on the RF phase at which they enter the grids, the accelerating voltage they see is different. Such complex distributions are commonly encountered in CCP plasmas where they occur for a similar reason.^{10,12} As the frequency increases above 5 MHz, a separated low-energy peak is seen in the distribution. This peak is formed from charge-exchange ions created in the downstream plume, or low-energy ions created due to ionization by any escaping electrons. As the frequency increases further, this low-energy peak becomes more and more distinct with an increasing separation distance from the main ion population.

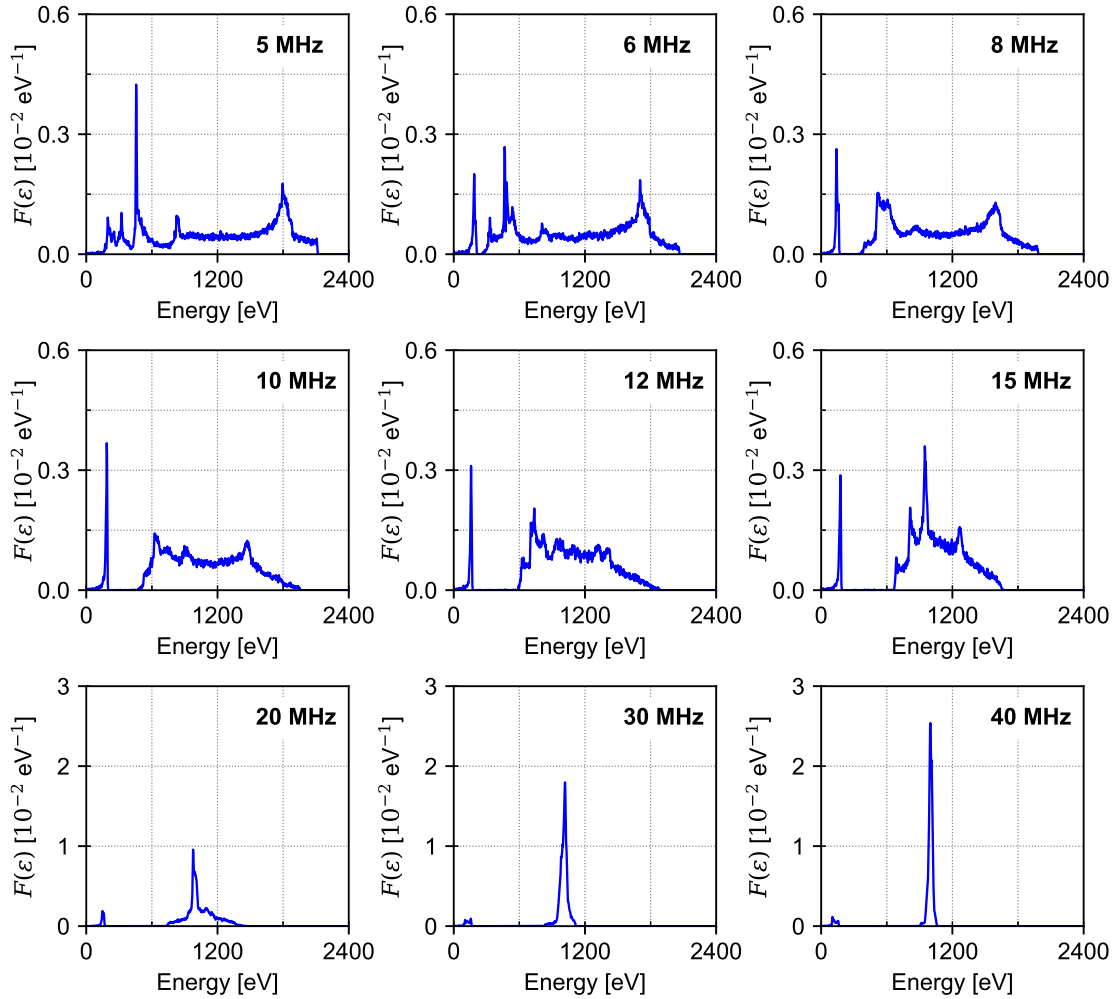


Figure 8. Time-averaged ion flux distribution functions (in energy units) measured on the downstream dielectric boundary surface at the frequencies indicated. The RF voltage amplitude is 1000 V. Note the change in y -axis scale for the last row of subplots.

Further increases in the applied frequency cause the width of the main ion population to shrink, while at the same time, a single sharp peak develops that becomes increasingly dominant, until for a frequency of about 30 MHz or higher, only a single narrow peak is observed. At these higher frequencies, the RF period is now much less than the ion transit time through the grids, and so the ions are no longer able to follow variations in the applied RF voltage. Since the background gas pressure is low, ion-neutral collisions only

have a small impact, and so the ion distribution is very narrow and sharply-peaked. A small, well separated, peak is still observed at very low energies though. This peak is not centered on zero, because a sheath forms in front of the downstream dielectric boundary, and which consequently accelerates these background ions.

The effect of the applied RF frequency on the ion beam distribution can be quantified by calculating the average ion beam energy, the beam energy standard deviation, and the average beam divergence angle. Here, the beam is defined as all ions except those of the low-energy peak formed from ion-neutral charge-exchange collisions and downstream ionization. Figure 9 (a) shows the average ion beam energy, ε_{beam} , and the energy spread measured in terms of a standard deviation, σ_ε . As the applied frequency increases, the average beam energy decreases, and approaches the sum of the self-bias voltage (which is close to the applied RF voltage amplitude) and the upstream sheath potential drop, as indicated by the horizontal red dashed line. At low frequencies, since the ions are able to follow variations in the time-varying RF fields, ions which enter the grids at certain RF phases can be accelerated to energies higher than the time-averaged value. Thus the average energy at low frequencies is higher than the self-bias.

The spread of the ion beam distribution is shown by the open black squares in Fig. 9 (a). Here the trends observed previously in Fig. 8 are clearly seen: as the applied frequency increases, the beam energy spread decreases, and at high frequencies, the beam is very narrow and sharply-peaked.

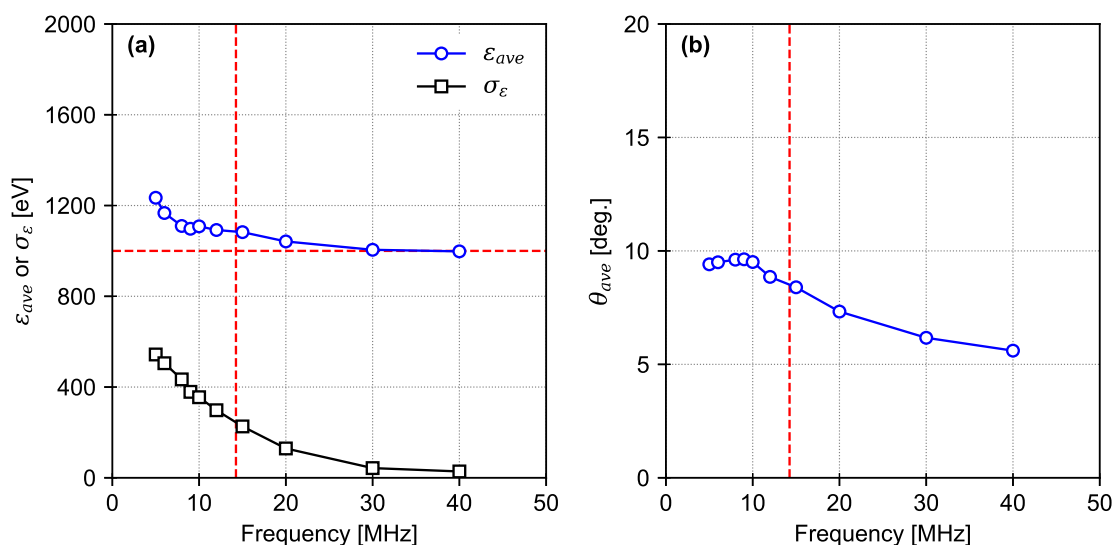


Figure 9. (a) Average ion beam energy and energy spread (quantified in terms of the standard deviation), and (b) average ion beam divergence angle as a function of the applied RF frequency. The vertical red dashed line shows the frequency (from Eq. 7) at which the ion transit time through the grids is equal to the RF period. The horizontal red dashed line in (a) shows the applied RF voltage amplitude which is 1000 V.

The ion beam also displays a spatial spread, which is determined by calculating the average incidence angle of ions on the downstream dielectric surface. At low frequencies the divergence angle is just below 10° , increasing slightly as the frequency increases and reaching a maximum at around 9 MHz. As the frequency further increases, ion beam focusing improves and the beam becomes increasingly collimated with the divergence angle decreasing towards 5° .

D. Plume potential

The applied frequency also plays an important role in determining the downstream plume potential. In conventional DC GITs, the neutralizer potential is chosen as the ground reference potential, and the plume is typically a few tens of voltage above this. The accel grid is then biased negatively with respect to the plume, so as to prevent electrons from backstreaming into the thruster. Choosing the potential of the bulk plume as the ground reference, Fig. 10 shows the time-averaged potential along the central hole axis (i.e. within the beamlet of each set of grid holes), as well as the potential between each set of grid holes (i.e. between the beamlets) at a low frequency of 5 MHz, and a high frequency of 40 MHz. As seen, despite the fact that only the voltage across the grids is controlled, the plume potential develops in such a way as to

ensure that the accel grid potential is negative with respect to the plume. Furthermore, the plume potential is higher than the central hole potential (which shows the characteristic saddle point). These results are very similar to those commonly encountered in conventional GITs, where the plume potential prevents excess electron backstreaming into the thruster,^{1,21,22} and demonstrates that in RF biased thrusters, a potential barrier naturally, and self-consistently, forms downstream of the accel grid.

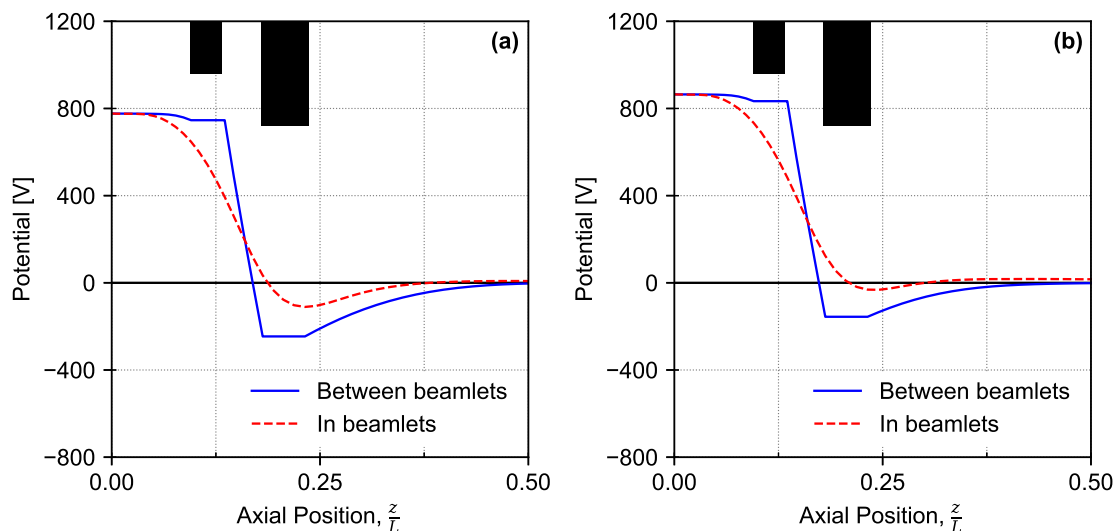


Figure 10. Spatial profile of the time-averaged potential (relative to the bulk plume potential) at an applied frequency of (a) 5 MHz, and (b) 40 MHz. The solid blue curves show the potential along an axial line between individual beamlets, while the dashed red lines show the potential within individual beamlets. The black rectangles denote the location of the grids. The RF voltage amplitude is 1000 V.

The potential profiles for both frequencies in Fig. 10 show similar behaviour, but the plume potential relative to the accel grid is higher at the lower frequency. This indicates slightly worse plume neutralization; as expected from Eq. 9. The potential along the hole axis for the high frequency case has a saddle point whose potential relative to the plume is slightly lower than at the lower frequency. The potential between the accel grid and plume acts to decrease the ion energy, in much the same way as in conventional GITs. There, it is also common to define the ratio of the net accelerating voltage (which is approximately equal to the screen grid potential) to the total acceleration voltage (given by the potential drop across the screen and accel grids). To prevent electron backstreaming, this ratio is usually between 0.8 - 0.9.¹ Based on the values of the plume potential in Fig. 10, the time-averaged net-to-total accelerating voltage ratio is found to be between about 0.75 - 0.85, which is again not too dissimilar to conventional DC GITs.

Figure 12 shows the time variation of the plume potential over two RF periods for frequencies of 5 MHz and 40 MHz, together with an overlay of the voltage applied across the screen and accel grids. As seen, the temporal variation is relatively complicated, and at 5 MHz, the maximum plume potential reaches a value as high as 400 V. By contrast, at 40 MHz the potential is relatively flat. When the applied voltage across the grids collapses, the plume potential immediately decreases due to the escaping electrons. For the 5 MHz case, the potential continues to decrease after the electrons stop escaping, as the density perturbation in the ion beam (resulting from the ion dynamics through the grids at this low frequency) continues to move further downstream (spreading in the process). For the high frequency case (and to a lesser extent, the lower frequency case), very high-frequency oscillations (with a frequency of about 800 MHz) are seen once the voltage collapses and electrons escape into the plume. Due to the higher potential in the accel grid hole compared with the upstream plasma source, escaping electrons are accelerated to form a beam (with an energy of about 100 - 200 eV), and some of the electrons in this beam are found to oscillate back and forth between the sheath in front of the downstream dielectric boundary (or ambipolar potential in space) and the potential between the plume and the accel grid.⁹ Thus, these oscillations are related to an electron transit time phenomenon in the downstream region (the transit time is of the order of 1 - 2 ns, which corresponds to a bounce frequency of about 500 - 1000 MHz). The decrease in plume potential (synchronised with the RF voltage), has been observed experimentally¹⁴ with electrostatic probes, while evidence of escaping electrons

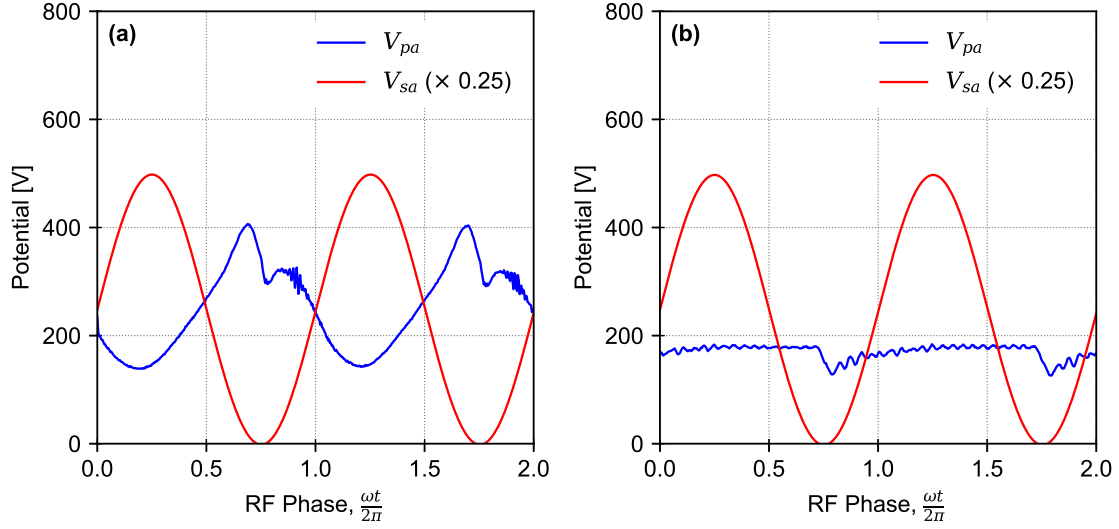


Figure 11. Time variation of the plume-to-accel grid potential during two RF periods for an applied frequency of (a) 5 MHz, and (b) 40 MHz. The red curves shows the RF voltage across the screen and accel grids (multiplied by a factor of 0.25) at the corresponding RF phase. The RF voltage amplitude is 1000 V.

has been observed based on light emission measurements with a high-speed camera (indicating the presence of high-energy electrons escaping the plasma source and subsequently producing downstream excitation and ionization).

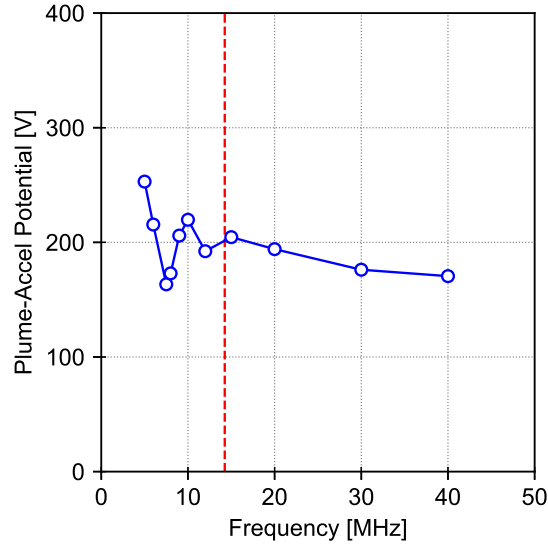


Figure 12. Time-averaged plume-to-accel grid potential as a function of the applied RF frequency. The vertical red dashed line shows the frequency (from Eq. 7) at which the ion transit time through the grids is equal to the RF period. The RF voltage amplitude is 1000 V.

As a measure of the level of downstream plume neutralization, we plot the time-averaged plume potential relative to the accel grid in Fig. 12. Overall, the potential decreases with the applied frequency, as anticipated from Eq. 9, with the potential going from around 250 V at 5 MHz, to about 175 V at 40 MHz. Since the energy of downstream ions that strike the accel grid is determined by the plume-to-accel grid potential, the applied frequency has an important effect on the erosion rate, and hence lifetime, of the accel grid. Interestingly, a type of resonance is observed in the potential for frequencies around 7.5 MHz, and the potential reaches a minimum of about 175 V. The exact cause of this resonance is not yet understood, but as

it occurs for frequencies where ion focusing is poor (see Section IV B), it is not a feasible operating region for the present thruster. Finally, the voltage difference (not shown) between the accel grid and the downstream dielectric boundary (which is essentially equivalent to the potential between the thruster and the vacuum chamber during ground testing), is found to be negative with a magnitude of about 20 - 30 V.

V. Variation of self-bias and ion focusing with RF voltage amplitude

In Section IV, the effect of the applied RF frequency was studied. Here we now briefly study the effect of the applied RF voltage amplitude, with the main aim of verifying the analytical theory (i.e. Eq. 2) presented in Section II. Figure 13 (a) shows the self-bias from the simulations at equilibrium for frequencies of 5 MHz and 40 MHz respectively as a function of the applied RF voltage amplitude. Also shown is the theoretical prediction (i.e. $V_{sb} \sim V_{rf}$). As seen, the simulation results for both frequencies are in excellent agreement with the theoretical predictions, and verify that the self-bias voltage is directly proportional to the RF voltage amplitude. Combined with the results of Section IV A, the results in this paper confirm the expected parametric scaling of the self-bias. The linear dependence of the self-bias with the applied voltage amplitude is also in good agreement with experimental measurements.^{7,8}

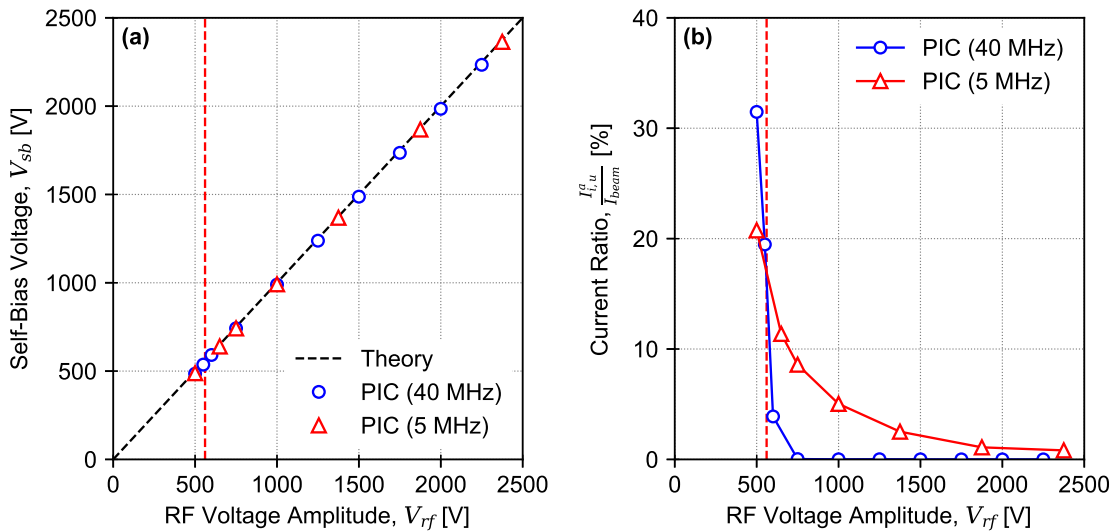


Figure 13. (a) Self-bias voltage, and (b) total ion current to the upstream accel grid surface (normalized by the ion beam current) as a function of the applied RF voltage amplitude. The black dashed line in (a) shows the approximate theoretical prediction from Eq. 4, while the vertical red dashed lines in (a)-(b) shows the perveance limit of the grids from Eq. 5.

Figure 13 (b) shows the total ion current to the upstream accel grid surface as a function of the applied RF voltage amplitude. For the high frequency of 40 MHz, the accel grid current is low; except for applied voltages below about 600 V. Using the DC Child-Langmuir law, the predicted perveance limit of the grids is also about 600 V. At 5 MHz however, although the ion current decreases with RF voltage amplitude, it is always greater than zero; even at those voltages where direct ion impingement is absent for the 40 MHz case. Thus, at low frequencies, no choice of applied voltage amplitude can prevent ion impingement. The current nonetheless decreases with the voltage amplitude, which is a consequence of the fact that as the amplitude increases, the portion of the RF period where the grid voltage is lower than the Child-Langmuir voltage decreases.

VI. Conclusions

In summary, it has been demonstrated that the applied frequency is a key parameter in RF biased thrusters that plays an important role in ensuring both good ion focusing through the acceleration grids, and a low plume potential. A lower frequency limit has been derived from simple physical considerations, and tested using PIC simulations, showing very good agreement. As long as the RF period is less than

the ion transit time through the grids, ions can be well focused and direct impingement of the accel grid eliminated. This transit time criterion gives a lower frequency limit of approximately 10 -15 MHz for typical grid dimensions and ion current densities. As the frequency is increased further, the ion beam velocity distribution becomes increasingly sharply peaked, and any RF modulation is minimized.

Observation of the thruster plasma potential, particularly in the near-plume region, shows a time-averaged profile that is very similar to that commonly seen in conventional DC GITs; the accel grid is negative with respect to the plume, and a potential barrier is formed that prevents excess electrons from backstreaming into the thruster. The plume-to-accel grid potential that self-consistently forms is approximately 20% of the total applied voltage across the grids, which is similar to the value chosen in conventional GITs. These results demonstrate that RF biasing of ion thruster grids is a feasible concept that can allow good ion focusing, a narrow ion beam velocity distribution, and inherent current balance with plume space charge compensation; all without the need for a separate neutralizer.

Acknowledgments

The authors would like to thank Stanislav Dudin for a number of useful discussions.

References

- ¹D. M. Goebel and I. Katz, *Fundamentals of Electric Propulsion: Ion and Hall Thrusters*, vol. 1. John Wiley and Sons, 2008.
- ²E. Stuhlinger, *Ion Propulsion For Space Flight*. McGraw-Hill New York, 1964.
- ³K. Nishiyama and H. Kuninaka, "Discussion on performance history and operations of hayabusa ion engines," *Transactions Of The Japan Society For Aeronautical And Space Sciences, Aerospace Technology Japan*, vol. 10, no. ists28, pp. Tb.1–Tb.8, 2012.
- ⁴S. Dudin and D. Rafalskyi, "On the simultaneous extraction of positive ions and electrons from single-grid icp source," *EPL (Europhysics Letters)*, vol. 88, no. 5, p. 55002, 2009.
- ⁵S. Dudin, D. Rafalskyi, and A. Zykov, "High homogeneity 25 cm low-energy rf ion source with inherent electron compensation," *Review of Scientific Instruments*, vol. 81, no. 8, p. 083302, 2010.
- ⁶S. Dudin and D. Rafalskyi, "A double-plasma source of continuous bipolar ion-ion beam," *Applied Physics Letters*, vol. 102, no. 3, p. 034102, 2013.
- ⁷D. Rafalskyi and A. Aanesland, "Coincident ion acceleration and electron extraction for space propulsion using the self-bias formed on a set of rf biased grids bounding a plasma source," *Journal of Physics D: Applied Physics*, vol. 47, no. 49, p. 495203, 2014.
- ⁸D. Rafalskyi and A. Aanesland, "Plasma acceleration using a radio frequency self-bias effect," *Physics of Plasmas*, vol. 22, no. 6, p. 063502, 2015.
- ⁹T. Laffeur and D. Rafalskyi, "Radio-frequency biasing of ion acceleration grids," *Plasma Sources Science and Technology*, vol. 27, no. 12, p. 125004, 2018.
- ¹⁰M. A. Lieberman and A. J. Lichtenberg, *Principles of Plasma Discharges and Materials Processing*. John Wiley & Sons, 2005.
- ¹¹P. Chabert and M. M. Turner, "A model for tailored-waveform radiofrequency sheaths," *Journal of Physics D: Applied Physics*, vol. 50, no. 23, p. 23LT02, 2017.
- ¹²P. Chabert and N. Braithwaite, *Physics of Radio-Frequency Plasmas*. Cambridge University Press, 2011.
- ¹³T. Laffeur, P. Chabert, M. Turner, and J.-P. Booth, "Theory for the self-bias formation in capacitively coupled plasmas excited by arbitrary waveforms," *Plasma Sources Science and Technology*, vol. 22, no. 6, p. 065013, 2013.
- ¹⁴J. Dedrick, A. R. Gibson, D. Rafalskyi, and A. Aanesland, "Transient propagation dynamics of flowing plasmas accelerated by radio-frequency electric fields," *Physics of Plasmas*, vol. 24, no. 5, p. 050703, 2017.
- ¹⁵J. P. Verboncoeur, A. B. Langdon, and N. Gladd, "An object-oriented electromagnetic pic code," *Computer Physics Communications*, vol. 87, no. 1-2, pp. 199–211, 1995.
- ¹⁶"Hayashi database, www.lxcat.net, retrieved on july 17, 2018."
- ¹⁷D. Piscitelli, A. Phelps, J. De Urquijo, E. Basurto, and L. Pitchford, "Ion mobilities in xe/ne and other rare-gas mixtures," *Physical Review E*, vol. 68, no. 4, p. 046408, 2003.
- ¹⁸I. Boyd and M. Crofton, "Grid erosion analysis of the t5 ion thruster," in *37th Joint Propulsion Conference and Exhibit*, p. 3781, 2001.
- ¹⁹J. Emhoff and I. Boyd, "Grid erosion modeling of the next ion thruster optics," in *39th AIAA/ASME/SAE/ASEE Joint Propulsion Conference and Exhibit*, p. 4868, 2003.
- ²⁰C. Farnell, J. Williams, and P. Wilbur, "Next ion optics simulation via ffx," in *39th AIAA/ASME/SAE/ASEE Joint Propulsion Conference and Exhibit*, p. 4869, 2003.
- ²¹Z. Lingwei, L. Yu, L. Juan, G. Zuo, J. Haocheng, W. Haixing, and T. Haibin, "Numerical simulation of characteristics of cex ions in ion thruster optical system," *Chinese Journal of Aeronautics*, vol. 23, no. 1, pp. 15–21, 2010.
- ²²S. Anbang, M. Genwang, Y. Juan, X. Guangqing, C. Maolin, and H. Chao, "Particle simulation of three-grid ecr ion thruster optics and erosion prediction," *Plasma Science and Technology*, vol. 12, no. 2, p. 240, 2010.